

Petrogenesis and geochemical characteristics of pyroxenite dykes in and around Salem Mafic–Ultramafic complex, southern India: an arc-related origin of Alaskan-type

Thoti Yellappa*

CSIR-National Geophysical Research Institute, Hyderabad 500 007, India

Arc-related origin of pyroxenites in association with Alaskan-type tectonics has been described in many mafic–ultramafic complexes across the globe. The Salem Mafic–Ultramafic Complex (SMUC) is one such Neoproterozoic Alaskan-type complex exposed at the northern margin of the Cauvery Suture Zone (CSZ), Southern Granulite Terrane, south India. The Complex consists of mafic and ultramafic sequences along with several occurrences of pyroxenite intrusions of varied thickness in the form of dykes. Similar pyroxenite dykes were also observed in and around the Complex at several locations within the basement hornblende gneiss, trending in the NE–SW and E–W directions. Petrography of these dykes indicated websterite variety with cumulate textures and reveals the dominance of clinopyroxene along with orthopyroxene, primary amphibole, minor plagioclase and oxide minerals like magnetite, ilmenite and spinels. The whole-rock chemistry of 10 representative samples showed enrichment of LILE elements (Sr, K, Rb, Th) and depletion of HFSE (Hf, Ti, Y, Yb) with normalized primitive mantle and N-MORB. The clinopyroxene mineral chemistry represented tholeiitic signatures with high Mg# values ($Mg/(Mg + Fe)$) up to 0.91, and the two-pyroxene thermobarometry of these pyroxenites yielded re-equilibrium crystallization temperatures of 820–932°C with moderate pressures at 11–12 kbar. Various tectonic discrimination plots of clinopyroxene mineral chemistry together with whole-rock chemistry favoured their origin under arc settings with the interactions of fluid-related subduction zone metasomatism relevant to Neoproterozoic Alaskan-type tectonics.

Keywords: Arc tectonics, geochemical characteristics, mafic–ultramafic complex, petrogenesis, pyroxenite dykes.

PYROXENITE intrusions are common constituent lithologies in mafic–ultramafic complexes. Several views have been presented regarding their origin, e.g. metamorphic segregation of the host peridotite entrappings, remnants of subducted oceanic crust and melt-rock replacement re-

actions between older pyroxenites and peridotites and percolating melts^{1–3}. Another view about their origin is that they occur as high-pressure crystal segregates of magmas by melting the subducted oceanic plate. It has also been reported that they form as crystal precipitates from asthenosphere-derived silicate magmas passing through the lithosphere^{4,5}. These rock types are commonly associated with stratiform complexes, Alpine-type/ophiolite complexes and Alaskan-type complexes. In Alaskan-type complexes, the pyroxenites are important intrusive rocks associated with dunite, peridotite and mafic assemblages like gabbro, gabbroic anorthosite and basalt/amphibolite⁶. The Alaskan-type complexes are designated as ‘zoned’ ultramafic complexes, commonly emplaced in convergent plate margin settings⁶ and have evolved from the Neoproterozoic to the Cenozoic periods with unique geodynamic settings. They act as hosts for a platinum group of elements (PGEs) and nickel–chromium mineralization^{7,8}. They constitute common mineralogy of ultramafic cumulate sequences like olivine, clinopyroxene, hornblende, plagioclases and rarely orthopyroxenes in association with accessory minerals of magnetite and ilmenite–chromites⁶. Geochemically, these complexes are tholeiitic in composition and their SiO₂ content ranges from 39.4% to 57.4% (ref. 6). They are enriched in large ion lithophile element contents (LILE) content and depleted in high field strength elements (HFSEs) along with moderate enrichment of light rare earth elements (LREs)^{7,9,10}. It was also inferred that these ultramafic–mafic intrusions involved Mg-rich hydrous parental magma from the subduction fluid-metasomatized lithospheric mantle source followed by subsequent crystal fractionation–accumulation processes⁷. The tectonic setting of these Alaskan-type complexes reveals that they tend to represent the products of subduction-derived arc magmas and/or arc-root complexes^{7,9–14}.

The Southern Granulite Terrane (SGT) consists of various lithological assemblages, which evolved in different magmatic and tectonic events from the Archean to Neoproterozoic periods. The mafic–ultramafic complexes of SGT are mostly restricted to the Cauvery Suture Zone (CSZ) and a few occur at its northern margin (Figure 1 a). The important ones include: (i) Bhavani–Mettupally Ultramafic

*e-mail: yellappa_thoti@yahoo.co.uk

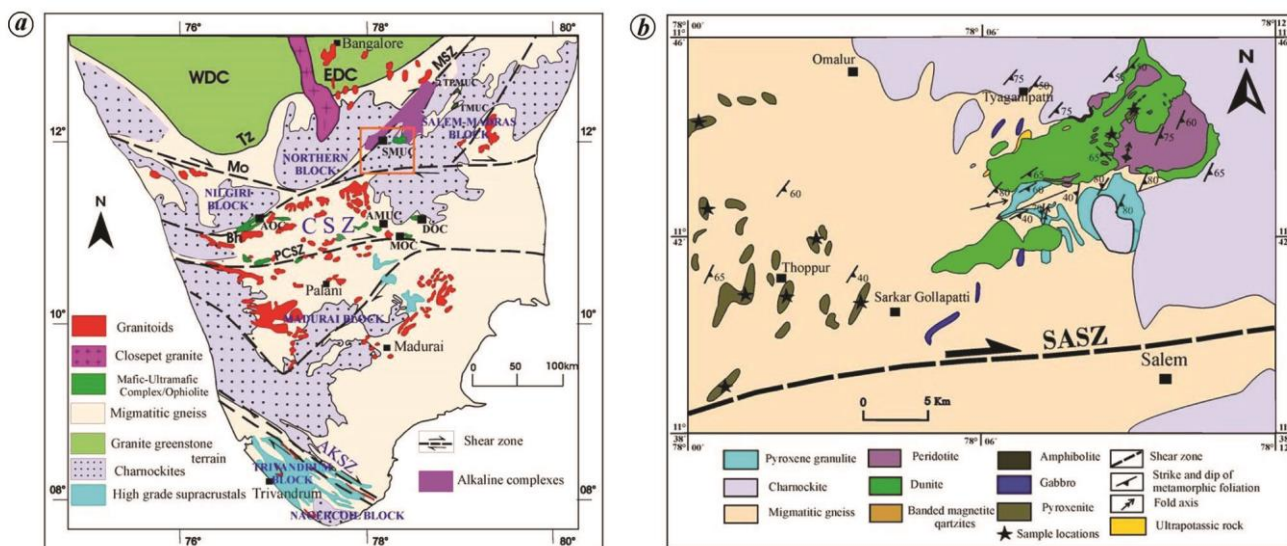


Figure 1. *a*, Geological map of Southern Granulite Terrane (SGT), modified after ref. 78: WDC, Western Dharwar Craton; EDC, Eastern Dharwar Craton; Tz, Transition Zone; CSZ, Cauvery Suture Zone; PCSZ, Palghat–Cauvery Shear Zone; MSZ, Moyar Shear Zone; Mo, Moyar; Bh, Bhavani; AKSZ, Achankovil Shear Zone; SMUC, Salem Mafic–Ultramafic Complex; SAC, Sittampundi Anorthosite Complex; AMUC, Aniyapuram Mafic–Ultramafic Complex; MOC, Manamedu Ophiolite Complex; DOC, Devanur Ophiolite Complex and box represents the study area. *b*, Geological map of SMUC and the adjoining regions showing pyroxenite intrusions and various lithological assemblages (modified after ref. 39 and published Geological Survey of India maps).

Complex (BMUC), (ii) Sittampundi Anorthosite Complex (SAC), (iii) Salem Mafic–Ultramafic Complex (SMUC), and some ophiolite complexes like Devanur, Manamedu, Aniyapuram and Agali^{15–21} (Figure 1). SMUC, known for its magnesite mineral potential, is located ~7 km north of Salem town, Tamil Nadu, India, which is at the northern margin of the CSZ. The Complex comprises serpentinized dunite, peridotite, pyroxenite, hornblendite, gabbro, amphibolite, mafic granulite, quartz monzonite and ultrapotassic rocks like shonkinite intrusions¹⁵. Recently, the tectonic evolution history of the Complex has been described as Neoproterozoic Alaskan-type origin²². At several locations in SMUC, numerous meter-scale pyroxenite dykes have intruded into the peridotite, serpentinized dunite and hornblende gneisses in around the complex. They occur in the form of elongated to curvilinear dykes of varying thickness and length (Figure 1 *b*) and trend in several directions, but dominantly along NE–SW in the proximity of CSZ. The present study focuses on the detailed field, petrological, whole-rock geochemistry and mineral chemistry of pyroxenites in and around SMUC, and aims to understand their spatial relationship, origin and tectonic evolution and similarity with Neoproterozoic Alaskan-type evolution. The results provide insights into the characteristics of the southern margin of the Dharwar Craton.

Geological setting

The SGT represents a classic Precambrian high-grade terrane, subjected to multiple tectono-thermal events like sub-

duction–collision tectonics, crustal anatexis and intrusions of ultramafic–mafic to felsic rocks with more polyphase metamorphic events^{23,24}. SGT preserves a vast Archean–Proterozoic crust of extensive high-grade granulite facies rocks like charnockites, two pyroxene granulites, associated hornblende granitic gneisses and granitoid rocks^{17,23} (Figure 1). Based on the structure and isotopic evolution history, the terrane has been broadly distinguished into six crustal blocks from the north to south, viz. (i) Northern Block, (ii) Nilgiri Block, (iii) Salem–Madras Block; (iv) Madurai Block, (v) Trivandrum Block and (vi) Nagercoil Block^{25–28} (Figure 1 *a*). The detailed geology and tectonics of these blocks have been described by several workers^{16,25–27}. The terrane is pierced with two major tectonic features: (i) E–W trending CSZ in the north divides southern India into two discrete tectonic blocks, viz. Dharwar Craton in the north and SGT in the south^{16,29}, and (ii) NE–SW trending Achankovil Shear Zone (AKSZ) in the south and southwest of the terrane, which separates the Madurai and Trivandrum blocks. Based on the age equivalents and tectonic relationships of several lithologies from CSZ, it is described as the Cambrian suture of Gondwana and also known as the Archean–Proterozoic Terrane boundary^{26,27}. Recently, numerous dismembered Neoproterozoic ophiolites have been reported from CSZ, namely Manamedu Ophiolite Complex (MOC)^{18,30}, Devanur Ophiolite Complex (DOC)¹⁹, Aniyapuram Mafic–Ultramafic Complex (AMUC)²⁰ and Agali Ophiolite Complex (AOC)²¹. These ophiolite complexes consist of a complete dismembered sequence of dunite, peridotite, pyroxenite, hornblendite, gabbro, gabbro norite, anorthosite, mafic

dyke, amphibolite, plagiogranite/trondhjemite and a thin pile of ferruginous chert. The ultra-high temperature metamorphic rocks and associated granulite-facies assemblages like orthopyroxene-bearing granulites, sapphirine-bearing rock and calc-silicates have also been reported within CSZ^{31,32}. The petrogenesis and geochemistry of these complexes suggest that they are mantle-derived arc magmas evolved under supra-subduction zone tectonic settings^{18–21}. The age of these complexes ranges from Neoproterozoic to Neoproterozoic periods: gabbros and plagiogranites of MOC (737 ± 23 to 782 ± 24 Ma and 744 ± 11 to 786 ± 7.1 Ma)³⁰; trondhjemites of DOC (2528 ± 61 to 2545 ± 56 Ma)¹⁹; metagabbros of AOC (2547 ± 17 Ma to 2547 ± 7.4 Ma)²¹; and metagabbros of AMUC 2436 ± 22 Ma (ref. 33).

The SMUC is located in the Salem–Attur Shear Zone (SASZ) (Figure 1 b), which represents the northern margin of CSZ, separating the Dharwar Craton to the north and SGT to the south. A network of several small-scale, narrow, shear zones trending NE–SW to N–S emerges from SASZ, traversing towards the north with intense tectonic fabrics (Figure 2 a). Based on different kinematic indicators and the structural history, SASZ has been described as a transpressional–dextral strike–slip shear zone^{34–36}. It has been recently described as a 10 km thick, low-angle thrust zone³⁷ and some workers have also described it as a vertical fault based on its predominant down-dip stretching lineations³⁸. The shear zone is marked by gently dipping mylonitic foliations with sub-horizontal lineations, S–C fabric structures, mantled porphyroclasts and intragranular faults. Based on the apparent offset position of structural grains between the Billirangan and Nilgiri Hills, earlier workers have also interpreted SASZ to be a dextral strike–slip shear zone²⁹. The dominant lithologies within SASZ and the adjacent region are represented by charnockite group of rocks, hypersthene gneisses, two-pyroxene granulites, quartzo–feldspathic granulites, migmatitic gneiss, phyllonites, banded magnetite quartzites, mafic–ultramafic rocks and ultrapotassic dykes¹⁷. These high-grade assemblages are extensively developed in the northern and northeastern parts of SASZ in the form of prominent hill ranges such as Shevroy hills, Yercaud hills and Kalrayan hills. Two-pyroxene granulites are the major rock type in this region; they are grey in colour and fine-to medium-grained with a typical ‘salt and pepper’ texture on the weathered surface. They consist of essential minerals such as diopside, hypersthene hornblende, and biotite along with minor amounts of quartz and plagioclase feldspar. Pyroxenite dykes occur in the form of elongated ridges of about 1–5 m height and of 3–5 m width, dominantly trending in the NE–SW direction. These are mostly located in the western part of SMUC around Toppur, south of Omalur, Tolur, Tirumalgriri village, and around Salem Steel Plant (Figure 2 b and c). They are sheared and metamorphosed, and show sharp contact with the basement hornblende gneiss. In the field, they are massive, coarse-to fine-grained with dark grey to light greenish colour

(Figure 2 c). In SMUC, they are associated with serpentinized dunite, peridotite and hornblendites in the form of very thin to thick layers (Figure 2 d).

SMUC, popularly known as Chalk Hills of Salem/Salem Magnesite Complex, is about 7 km from Salem town in the north and is well known for magnesite mining. SMUC structurally overlies the older migmatitic gneiss surrounded by high-grade assemblages like charnockites and two-pyroxene granulites (Figure 1 b). The complex occurs as two intrusive bodies separated by gneisses, and granulites, and

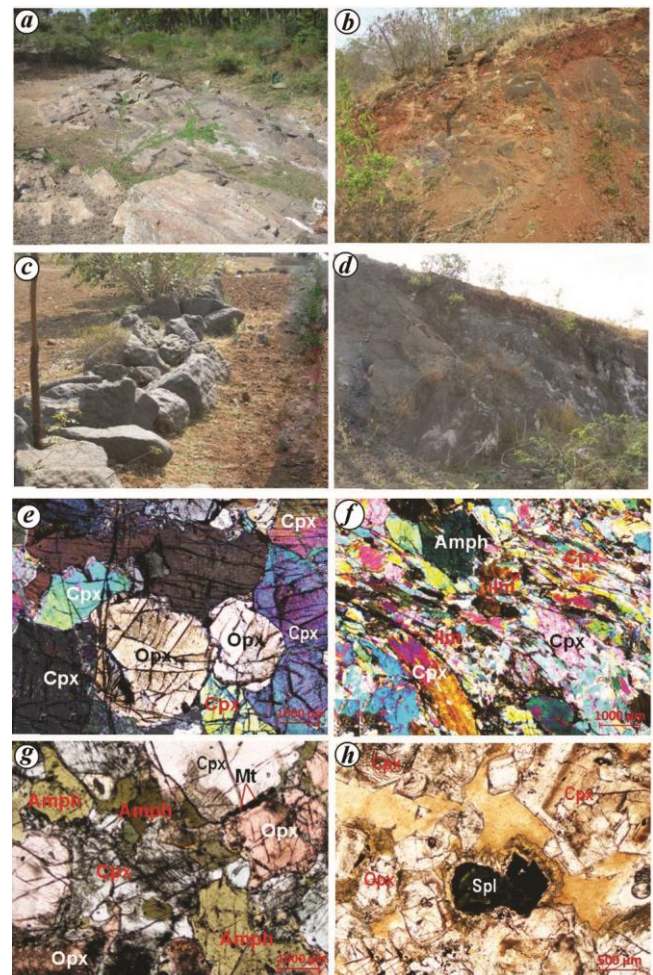


Figure 2. Field photographs and thin section microphotographs of studied pyroxenite dykes and adjacent rocks in and around SMUC. **a**, A highly deformed basement hornblende gneiss showing an intense tectonic fabric within the Salem–Attur Shear Zone. **b**, A thick intrusion of pyroxenite dyke along with big boulders near Thoppur village, west of Salem town. **c**, Very to fine-grained with dark grey to light greenish coloured pyroxenite vein near Tirumalgiri village, west of Salem town; the boulders are excavated and dumped from the agriculture fields. **d**, A thick vein of pyroxenite intruded into the serpentinized dunite at SMUC. **e**, Primary magmatic cumulus texture in pyroxenite, under XPL. **f**, Deformed grains of Cpx showing strong foliation fabric due to intense shearing in pyroxenite, under XPL. **g**, Presence of both primary and secondary amphiboles in pyroxenite, under PPL. **h**, Spinel with a dark greenish tinge in pyroxenite, under PPL. Cpx, Clinopyroxene, Opx, Orthopyroxene, Amph, Amphibole; Pl, Plagioclase; Mt, Magnetite; Ilm, Ilmenite; spnl, spinel; XPL, Crossed polarized light; PPL, Plane-polarized light; RFL, Reflected light.

both bodies are disposed in an en echelon fashion along the ENE–WSW direction parallel to the general foliation trend of basement gneisses. The larger one extends for about 26 sq. km area in the northern part and the smaller one extends for 4 sq. km areas in the southern part (Figure 1 *b*). The SMUC consists of a cumulate sequence of serpentized dunite dominantly in the centre, followed by layers of peridotite, olivine pyroxenite, wherlites, hornblendite, gabbro and amphibolite intrusions. Several ultrapotassic dykes like shonkinite and lamprophyre varieties of younger intrusions also occur around the Complex. The detailed geological history and their petrogenesis have been described by many workers^{15,22,39,40}. Based on the chrome spinel chemistry from dunites and peridotites and whole-rock geochemical characteristics of the amphibolites together with zircon U–Pb geochronology of quartz monzonites from the Complex, it is described as Neoproterozoic (~800 Ma) Alaskan-type²². Towards the west of SMUC in the basement gneiss, several thin dykes of pink syenites, basic dykes, quartz and pegmatite veins of younger emplacements were also observed, and these are structurally controlled.

Materials and method

Based on the field observations and published literature like Geological Survey of India maps and reports, a simplified geological map of the study area with detailed sketches was drawn (Figure 1 *b*). Twenty samples of less deformed and unaltered rocks from several dykes were collected for petrological and geochemical studies. After a detailed petrological study, 10 representative samples of pyroxenites were selected for whole-rock analysis. The samples were chipped manually using a hammer and cleaned by the process of ultrasonication with deionized water. Using a steel jaw crusher, the samples were crushed into coarse-grained pieces of <1 cm in length and pulverized to a fine powder using agate mortar. About 1–1.5 g of sample-pressed fine powder of pellets was prepared and the abundance of major elements was determined using WD-XRF (PANalytical Axios^{mAX}) at National Geophysical Research Institute, Hyderabad. To determine trace and REE concentrations, 0.50 mg of powder from each sample was taken in Savillex Teflon beakers along with a double-distilled acid mixture of HF + HNO₃ + HClO₄ + HCl and heated up to 48 h. After completely drying the samples, 10 ml of HNO₃ was added to each sample and diluted with double-distilled water with follow-up of standard procedures⁴¹. Rh was used as an internal standard. The analysis was performed using HR-ICP-MS (Nu instruments atom, UK) at NGRI. For both XRF and ICP-MS techniques, international rock standards were used for calibration. Table 1 shows the analytical results. Three samples of previous analytical results of pyroxenites of SMUC (earlier study²²) were considered references. For mineral chemistry, two representative pyroxenites

were chosen. Mineral analysis of clinopyroxene, orthopyroxene and amphiboles was performed on thin polished sections after proper carbon coating using Cameca SX-100 electron probe micro-analyser (EPMA) at NGRI. During analysis, the instrument maintained a 15 kV accelerating voltage with a probe current of 12 nA. The counting times of 40 sec for Si, Al, K, Na, Ca, Mg, Ti, Cr and Ni and 20 sec for Mn and Fe were followed. Data were reduced using ZAF (in JXA8621 and JXA-8200) and phi–rho–z (in SX100) correction methods. Major elemental compositions like SiO₂, Al₂O₃, TiO₂, NiO, Cr₂O₃, FeO, MnO, MgO, CaO, Na₂O, K₂O and P₂O₅ were estimated from the mineral cores. The following standards of natural and synthetic minerals include wollastonite–Ca–Si, aegirine–Na, K-feldspar–K, chromite–Cr, fayalite–Fe, corundum–Al, periclase–Mg, bunsenite–Ni, pyrolusite–Mn and rutile–Ti were used for calibration. The analytical results are given in Table 2 (average) and in the [supplementary material](#) (in detail).

Petrography

The pyroxenites in and around SMUC, in hand specimens, appeared dark greyish to light green in colour, and coarse-to fine-grained in nature. Under the microscope, most of them showed primary magmatic cumulus textures (Figure 2 *e*) with clinopyroxene (Cpx: 50–65%), orthopyroxene (Opx: 5–30%) and amphiboles (5–20%) occurring as common minerals along with oxide minerals like magnetite, ilmenite and spinels up to 1–2% in the rocks. The modal composition showed that they belonged to the websterite variety. Cpx was the dominant mineral, which was coarse-grained, exhibiting wavy extinctions and exsolution texture. In some samples, Cpx was strongly deformed and elongated (Figure 2 *f*). Strain effects were clearly visible (Figure 2 *f*), and both Cpx and Opx were anointed. The presence of reaction rims around Cpx was also noted in some samples. Opx was relatively less compared to Cpx and in some samples, an equal proportion of both Cpx and Opx were observed. Opx was euhedral to subhedral in shape, representing granulations of the phenocrysts of Cpx (Figure 2 *d*). In some places, Opx also showed strong deformation and was broken into sub-grains at the margins. Amphibole was mainly hornblende; it occurred as an interstitial phase between pyroxene crystals and as an alteration product of Cpx and Opx (Figure 2 *g*). Most of the amphiboles were primary hornblendes with wavy extinctions in a few samples and they were typically accompanied by opaque minerals like ilmenites and magnetite (Figure 2 *f* and *g*). In some samples, brown amphiboles were dominant. Feldspars were seen in minor amounts along the grain boundaries of both Cpx and Opx. Ilmenites are small, brownish-red in colour, anhedral to subhedral in shape with tiny inclusions of magnetite. In some samples, greenish-coloured spinels were also observed (Figure 2 *h*).

Table 1. Whole rock analysis of pyroxenites in and around the Salem Mafic–Ultramafic Complex (SMUC)

Rock type Sample no:	Pyroxenite									
	SL-4A	SL-55A	SL-55 D	SL-74 A	SL-2	SL-74 H	SL-56E	SL-55	SL-55 E	SL-9
SiO ₂	44.41	52.37	53.27	46.17	50.98	47.54	51.94	53.67	50.97	46.55
Al ₂ O ₃	5.61	3.07	2.96	6.96	7.56	6.17	1.93	2.73	2.65	3.49
FeO _i	8.47	9.82	6.64	14.98	9.71	10.26	12.85	8.82	8.77	8.38
MnO	0.15	0.23	0.19	0.23	0.23	0.22	0.19	0.20	0.23	0.15
MgO	21.42	16.59	15.96	18.07	18.93	16.58	17.98	16.35	15.13	24.5
CaO	15.13	15.17	17.63	8.60	9.56	16.15	10.32	15.36	19.02	13.4
Na ₂ O	0.85	1.01	0.57	2.38	0.98	1.14	1.27	1.07	0.54	0.6
K ₂ O	0.21	0.14	0.06	0.39	0.10	0.17	1.84	0.12	0.03	0.02
TiO ₂	0.38	0.24	0.20	1.09	0.41	0.49	0.27	0.19	0.40	0.41
P ₂ O ₅	0.02	0.05	0.02	0.16	0.02	0.05	0.09	0.03	0.02	0.05
LOI	2.8	0.97	1.31	0.09	1.54	0.26	0.30	0.67	1.49	2.1
Total	99.45	99.64	98.81	99.11	100.02	99.03	98.97	99.21	99.26	99.65
Sc	40.81	39.39	42.96	29.39	28.64	61.86	30.89	41.77	64.58	51.33
V	150.68	97.92	86.73	275.67	116.30	244.13	110.36	87.65	200.98	216.9
Cr	2285.00	1139.03	2174.27	1539.35	1596.92	1612.33	1342.76	1278.37	1391.98	2742
Co	29.03	59.82	49.54	91.26	51.44	62.52	68.22	60.76	57.09	19.09
Ni	675.00	351.28	377.57	876.65	380.11	268.67	459.94	361.89	273.46	138.5
Cu	54.40	9.89	17.30	151.08	31.42	9.03	18.14	10.62	13.09	22.09
Zn	13.04	114.37	104.35	166.36	125.66	182.29	285.93	106.22	175.92	244.4
Ga	14.29	6.07	3.69	15.12	7.99	8.37	7.39	5.30	6.53	7.14
Rb	0.79	1.22	1.12	12.77	1.00	2.59	85.08	2.98	1.22	0.085
Sr	238.11	120.05	77.67	118.75	18.58	87.87	487.36	138.69	134.08	15.1
Y	5.12	10.83	8.98	16.89	7.80	19.09	12.73	10.15	19.01	3.724
Zr	18.83	32.93	19.11	74.75	21.84	64.96	33.62	36.40	26.14	33.69
Nb	2.65	0.45	0.12	2.16	0.55	1.92	0.18	0.48	0.05	0.485
Cs	0.01	0.07	0.10	0.32	0.03	0.04	0.54	0.20	0.17	0.026
Ba	27.71	20.79	30.10	63.79	17.86	150.95	1072.31	22.80	28.38	10.99
Hf	1.43	1.01	0.62	2.06	0.62	1.42	1.04	1.02	0.92	1.013
Ta	0.07	0.11	0.02	0.22	0.15	0.13	0.02	0.14	0.02	0.054
Pb	0.80	7.29	9.50	12.20	8.58	7.25	14.44	8.65	11.23	2.795
Th	0.03	0.42	0.12	1.43	0.13	0.47	0.41	0.71	0.10	0.054
U	0.08	0.14	0.09	0.60	0.09	0.15	0.16	0.18	0.12	0.026
La	9.67	5.42	3.28	7.35	1.15	15.36	4.98	8.44	2.93	9.927
Ce	11.48	12.61	8.55	15.46	2.89	36.86	13.81	17.77	11.60	9.567
Pr	6.92	1.73	1.27	1.99	0.42	4.82	2.07	2.23	2.09	4.909
Nd	33.18	8.08	6.47	8.58	2.11	21.33	10.68	9.30	12.54	24.17
Sm	6.75	2.49	2.09	2.64	0.69	5.52	3.33	2.67	4.34	5.074
Eu	4.73	0.88	0.63	0.84	0.22	1.12	1.07	0.77	1.39	1.191
Gd	5.13	2.41	2.13	2.91	0.87	3.90	3.02	2.36	4.43	4.09
Tb	0.65	0.36	0.32	0.48	0.16	0.58	0.44	0.35	0.66	0.551
Dy	3.24	1.87	1.66	2.88	1.14	3.08	2.19	1.78	3.48	2.548
Ho	0.73	0.36	0.31	0.56	0.25	0.61	0.41	0.34	0.65	0.355
Er	2.21	0.87	0.77	1.44	0.68	1.62	1.05	0.86	1.64	1.104
Tm	0.13	0.13	0.11	0.20	0.11	0.23	0.15	0.12	0.23	0.18
Yb	1.56	0.83	0.69	1.31	0.72	1.53	0.96	0.78	1.46	0.961
Lu	0.41	0.12	0.10	0.18	0.11	0.22	0.13	0.11	0.20	0.167
Total REE	91.14	38.14	28.38	46.82	11.52	96.79	44.30	47.86	47.64	64.794
Mg# 100*MgO/(MgO + FeO)	71.66	62.81	70.61	54.68	66.09	61.78	58.32	64.96	63.30	74.51
Fe# = 100*FeO/(FeO + MgO)	28.34	37.19	29.39	45.32	33.91	38.22	41.68	35.04	36.70	25.49
Al ₂ O ₃ /TiO ₂	14.76	12.82	14.95	6.41	18.31	12.64	7.24	14.37	6.55	8.51
Na ₂ O + K ₂ O	1.06	1.15	0.63	2.77	1.08	1.32	3.11	1.19	0.57	0.62
Na ₂ O/K ₂ O	4.05	7.33	9.55	6.14	9.47	6.56	0.69	9.15	18.66	30.00
Zr/Nb	7.11	73.07	157.97	34.66	39.42	33.85	189.09	75.63	490.37	69.46
La/Nb	3.65	12.02	27.11	3.41	2.08	8.01	28.03	17.54	54.98	20.47
Th/La	0.00	0.08	0.04	0.19	0.11	0.03	0.08	0.08	0.03	0.01
Nb/Th	101.92	1.08	1.03	1.51	4.40	4.07	0.43	0.68	0.55	8.98
Zr/Y	3.68	3.04	2.13	4.43	2.80	3.40	2.64	3.59	1.38	9.05
Lu/Hf	0.28	0.12	0.16	0.09	0.17	0.15	0.13	0.11	0.22	0.16
Ce/Pb	14.35	1.73	0.90	1.27	0.34	5.08	0.96	2.05	1.03	3.42
La/Yb _N	4.289	4.545	3.276	3.891	1.115	6.968	3.608	7.494	1.391	7.165
Sm/Nd _N	0.625	0.949	0.993	0.947	1.002	0.795	0.959	0.882	1.063	0.645

(Contd)

Table 1. (Contd)

Rock type	Pyroxenite									
	SL-4A	SL-55A	SL-55 D	SL-74 A	SL-2	SL-74 H	SL-56E	SL-55	SL-55 E	SL-9
Sample no:										
Ce/Yb _N	1.984	4.124	3.329	3.188	1.087	6.515	3.898	6.147	2.145	2.691
La/Sm _N	0.896	1.360	0.982	1.739	1.049	1.742	0.936	1.979	0.423	1.224
Gd/Yb _N	2.714	2.415	2.543	1.837	1.004	2.110	2.610	2.503	2.511	3.521
Eu/Eu*	2.348	1.072	0.899	0.918	0.850	0.696	1.003	0.910	0.954	0.769
La/Gd _N	1.581	1.882	1.288	2.118	1.111	3.302	1.382	2.994	0.554	2.035
Gd/Lu _N	1.536	2.490	2.679	1.925	1.000	2.182	2.728	2.622	2.651	2.984

Table 2. Mineral analysis of pyroxenites in and around SMUC (averages)

Sample no.	SL-9	SL-4	SL-9	SL-4	SL-4
Mineral	Cpx	Cpx	Opx	Opx	Amp
No. of analyses (average)	13	10	4	8	7
SiO ₂	50.73	48.83	50.71	51.26	41.63
TiO ₂	0.40	0.24	0.05	0.04	1.05
Al ₂ O ₃	4.08	5.51	2.25	4.42	13.54
Cr ₂ O ₃	0.30	0.18	0.12	0.12	0.29
FeO	5.32	5.59	13.57	13.79	8.46
MnO	0.13	0.14	0.26	0.30	0.11
MgO	14.10	13.36	25.82	27.27	14.96
CaO	21.89	22.42	1.56	0.38	11.77
Na ₂ O	1.30	1.10	0.12	0.02	2.29
K ₂ O	0.01	0.00	0.00	0.01	0.73
P ₂ O ₅	0.02	0.02	0.02	0.01	0.02
NiO	0.04	0.04	0.08	0.09	0.12
ZnO	0.01	0.02	0.05	0.06	0.05
Total	98.32	97.44	94.60	97.78	95.04
No of oxygens	6	6	6	6	23
Si	1.903	1.859	1.933	1.882	6.141
Al _{iv}	0.097	0.141	0.067	0.118	1.848
Al _{vi}	0.084	0.106	0.034	0.073	0.513
Fe ⁺³	0.114	0.142	0.072	0.064	0.524
Cr	0.009	0.006	0.004	0.004	0.118
Ti	0.011	0.007	0.001	0.001	0.034
Fe ⁺²	0.058	0.035	0.355	0.358	0.521
Mn	0.004	0.004	0.008	0.009	0.014
Mg	0.788	0.757	1.468	1.493	3.287
Ca	0.880	0.912	0.064	0.015	1.862
Na	0.095	0.080	0.009	0.002	0.658
K	0.000	0.000	0.000	0.000	0.138
Total	4.037	4.046	4.015	4.018	15.658
Wo	47.876	49.387	3.194	0.763	
En	42.906	41.004	74.746	77.018	
Fs	9.219	9.609	22.060	22.218	
Mg# Mg/(Mg + Fe ⁺²)	0.933	0.956	0.806	0.807	0.867
Ca# Ca/(Ca + Na + K)	0.903	0.919			0.796
Temperature (°C)	880.00	889.00			
Pressure (kbr)	11.17	11.69			

Detailed data are provided in the [Supplementary Material](#).

Analytical results

Whole-rock chemistry

The pyroxenites showed moderate SiO₂ (44.41–53.27 wt%) and Al₂O₃ varied from 1.93 to 7.56 wt%. They showed relatively higher MgO (15.13–21.42 wt%) and FeO (6.64–12.85 wt%) content. The alkali content was relatively low

with Na₂O of 0.57–2.38 wt% and K₂O less than 1 wt%, except for one sample with 1.84 wt%. When compared with the pyroxenites of orogenic and ophiolitic sequences worldwide (Figure 3)⁴², they were richer in CaO (8.60–19.02 wt%) content with moderate TiO₂ (0.19–1.0 wt%). The trace element concentration was relatively higher; the Ni contents ranged from 274 to 877 ppm and Cr from 1139 to 2285 ppm. V varied from 87 to 278 ppm and Co from 29 to 92 ppm. The LIL elements such as Ba showed low to slightly high concentration (20.79–1072 ppm) and Sr from 19 to 487 ppm. Rb concentration was very low from (0.79–13 ppm; except for one sample of 85 ppm) and K/Rb ratio was relatively higher (179–936; one sample with a higher value of 2206). The incompatible trace elements like Nb, Ta and Hf were relatively low in abundance. However, zircon varied from 18.82 to 64.96 ppm, and the Zr/Y ratio ranged from 1.38 to 3.7. The Ti/Zr ratio ranged from 31 to 113, Nb/Th ratio from 0.43 to 4.4 (except one sample of 102) and Zr/Nb ratio from 7.11 to 189 (one sample of a higher ratio of 490). The total REE concentration of these pyroxenites was relatively higher (11.52–91.14). On the chondrite normalization spider plot, they showed progressive LREE enrichment (Figure 4a) and were strongly fractionated by both LREE and middle rare earth elements (MREE) ((La/Gd)_{CN} = 0.55–3.3). From MREE to heavy rare earth elements (HREE), they exhibited slightly negative slopes ((Gd/Lu)_{CN} = 1.0–2.71) along with negative Eu anomalies ((Eu/Eu*)_{CN} = 0.7–1.1; except for one sample of 2.34). The primitive mantle (PM) and N-MORB normalization of diagrams (Figure 4b and c respectively) of these pyroxenites represent strong enrichment in LILE such as Cs, Rb, Ba, K and also other fluid-mobile elements of Th, U and Pb (except a few samples) compared to the neighbouring lithophile elements. HFSE (Nb, Y, Zr, Hf and Ti) were strongly depleted in both PM and MORB normalization, particularly with low Zr ratios ((Zr/Hf)_{PM} = 0.36–1.3).

Mineral chemistry

Clinopyroxene: Cpx analysis was carried out for two samples (SL-4 and SL-9) and the results showed that these were highly Mg-rich with a nearly uniform concentration in terms of Fe–Mg ratio (Table 2). They exhibited higher Mg# of 0.84–0.98 (Mg# Mg/(Mg + Fe⁺)) and lower Ti

($\text{TiO}_2 = 0.11\text{--}0.53$ wt%) content. The Wo composition varied from 47.34 to 50.23 mol%, En from 40.0 to 45.18 mol% and Fs from 8.14 to 10.44 mol%. On the trilinear diagram of En–Wo–Fs (Figure 5a), all these clinopyroxenes plot in the diopside field only. These were rich in Ca and their Ca# ($\text{Ca}/[\text{Ca} + \text{Na} + \text{K}]$) ranged from 0.89 to 0.93 and relatively poor in alkalis ($\text{Na}_2\text{O} < 1.5$ wt%; $\text{K}_2\text{O} < 0.05$ wt%). They showed a significant concentration of SiO_2 (47.45–51.88 wt%) and Al_2O_3 (3.71–6.19 wt%). On the SiO_2 versus Al_2O_3 discrimination plot, they showed non-alkaline to normal alkaline signature (Figure 5b). Cr_2O_3 (0.13–0.36 wt%) and TiO_2 (0.11–0.53 wt%) were in almost equal proportions. On the Ti versus Al_t plot (Figure 5c), they showed the tholeiitic signature of their source magmas, while the Ti versus $\text{Ca} + \text{Na}$ plot (Figure 5d) represents their tholeiitic to alkali olivine basaltic nature. MnO ranged up to 0.22 wt%. The Mg# versus MnO plot represents a possible fractional crystallization trend of their magmas (Figure 5e). The Al_{vi} versus Al_{iv} discrimination plot (Figure 5f) of Cpx represents their evolution under medium pressure conditions⁴³.

Orthopyroxene: Opx analysis was carried out from the same two samples of less alteration. They showed the homogeneous composition of Fe–Mg ratio (Table 2) and magne-

sium content (Mg#) varied from 0.79 to 0.84. These were enstatitic in nature and showed slightly higher compositional ranges of En: 64.6–83.1 mol%, and lower concentration of Wo: 0.15–1.8 mol% (except one grain with a slightly higher content of 11.22 mol%), and average composition of Fs: 16.4–24.18 mol%. The SiO_2 and Al_2O_3 contents varied from 48.13 to 53.28 wt% and 2.1–4.57 wt% respectively. The TiO_2 contents were very low (0.02–0.1 wt%) and CaO was below 1 wt%, except for one grain with 5.48 wt%. The Na_2O and K_2O contents were less than 0.5 wt%. On the trilinear diagram of En–Wo–Fs (Figure 5a), these orthopyroxenes plot in the enstatite field.

Amphibole: Amphibole analysis was carried out from one sample (SL-4). Many of these are primary amphiboles which show slightly higher Mg# (0.79–0.92) and $\text{Na} + \text{K}^A$ in the range (0.4–0.9). Si ranged from 5.98 to 8.83 wt% and FeO from 7.88 to 9.81 wt%. Al_2O_3 varied from 6.51 to 15.94 wt% and Ca# was slightly higher (0.82 to 0.92) in these amphiboles. The Mg# versus Si and Al_{iv} versus ($\text{Na} + \text{K}$) plots (Figure 6a and b respectively) indicate that

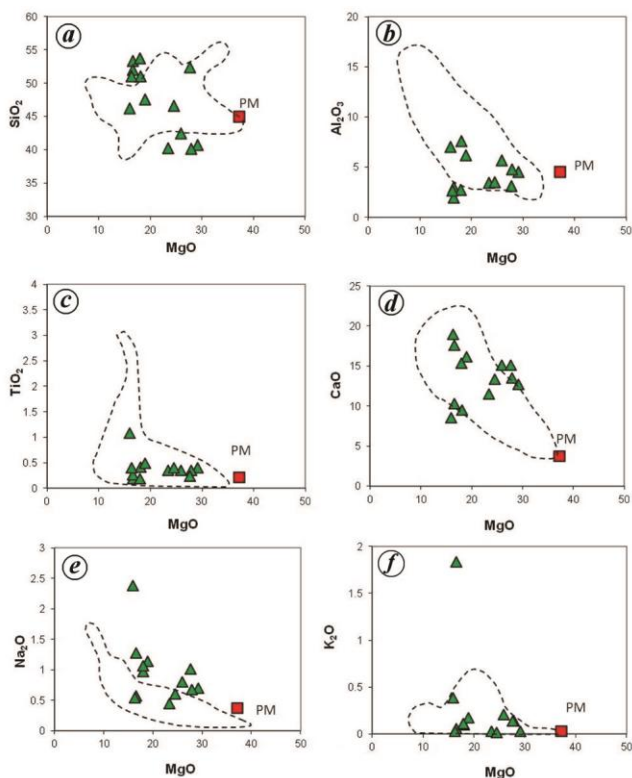


Figure 3. Binary variation diagrams of major oxides derived from whole-rock chemistry: MgO versus (a) SiO_2 , (b) Al_2O_3 , (c) TiO_2 , (d) CaO, (e) Na_2O and (f) K_2O concentration of pyroxenites in and around SMUC. Fields of a worldwide database of mantle pyroxenites (massifs and xenoliths) are shown for comparison^{42,79} (PM, Primitive Mantle).

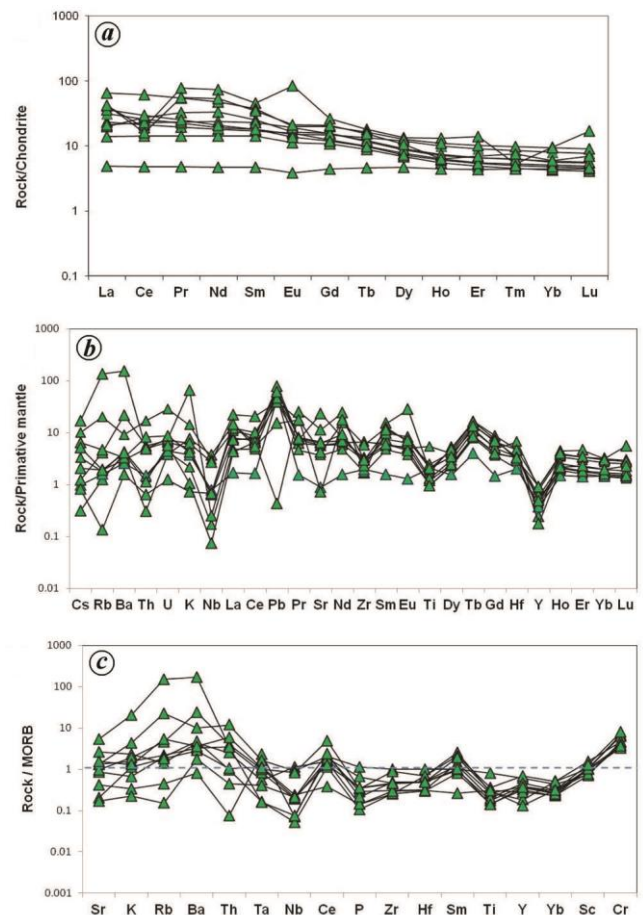


Figure 4. Spider plots of pyroxenites with normalizing factors. a, Chondrite normalization REE plot (normalized values⁸⁰). b, PM normalization plot of selected trace and REE (normalized values⁸⁰). c, MORB normalization incompatible elements plot (normalized values⁸⁰).

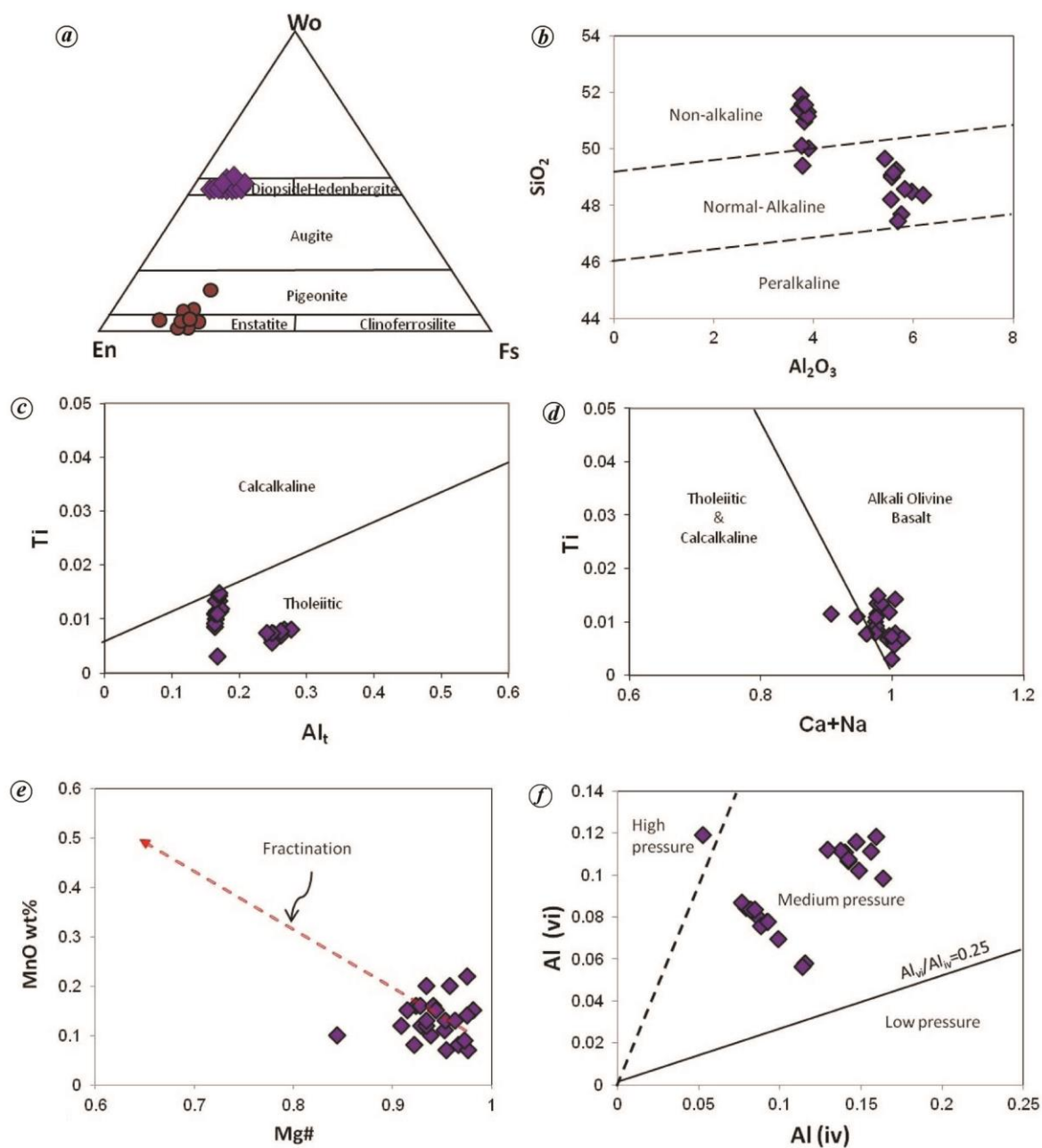


Figure 5. Mineral chemistry variation plots of Cpx and Opx from the pyroxenites in and around SMUC. *a*, Wo–En–Fs classification plot for both pyroxenes⁸¹, diamond represents Cpx and circle represents Opx. *b*, SiO₂ versus Al₂O₃ binary diagram for Cpx classification⁵⁹. *c*, Ti versus Al, classification plot for Cpx⁶¹. *d*, Ti versus Ca + Na classification plot for Cpx⁶¹. *e*, MnO versus Mg# classification plot for Cpx⁸². *f*, Plot of relative proportions of Al in the tetrahedral site and Al in the octahedral sites of Cpx for pressure estimation⁸³. The diamond represents Cpx and the circle represents Opx.

these amphiboles belong to the pargasite group, except for one grain plotted in the edenite field, possibly due to breakdown rim. NiO ranged from 0.02 to 0.21 wt%. On the Ca + Na + K versus Si diagram (Figure 6c)⁴⁴, their composition is plotted in the field of igneous amphiboles. Further, the (Na + K)^A versus Al_(IV), (Na + K)^A versus TiO₂, and (Na/Ca + Na) versus (Al/Si + Al) plots (Figure 6d–f respectively)⁴⁵, strongly resemble the primary amphibole trends.

Geothermobarometry: The studied rocks were subjected to deformation and high-grade metamorphism and hence there is a possibility of cation exchange of highly mobile elements (e.g. Ca, Na), which results in some compositional variations. There are several geothermobarometers available in the literature for these kinds of igneous rocks^{46,47}. In this study, for the estimation of temperature and pressure, two-pyroxene thermobarometry⁴⁷ and Cpx barometry⁴⁸ have been used. The Cpx with higher Mg# values (above

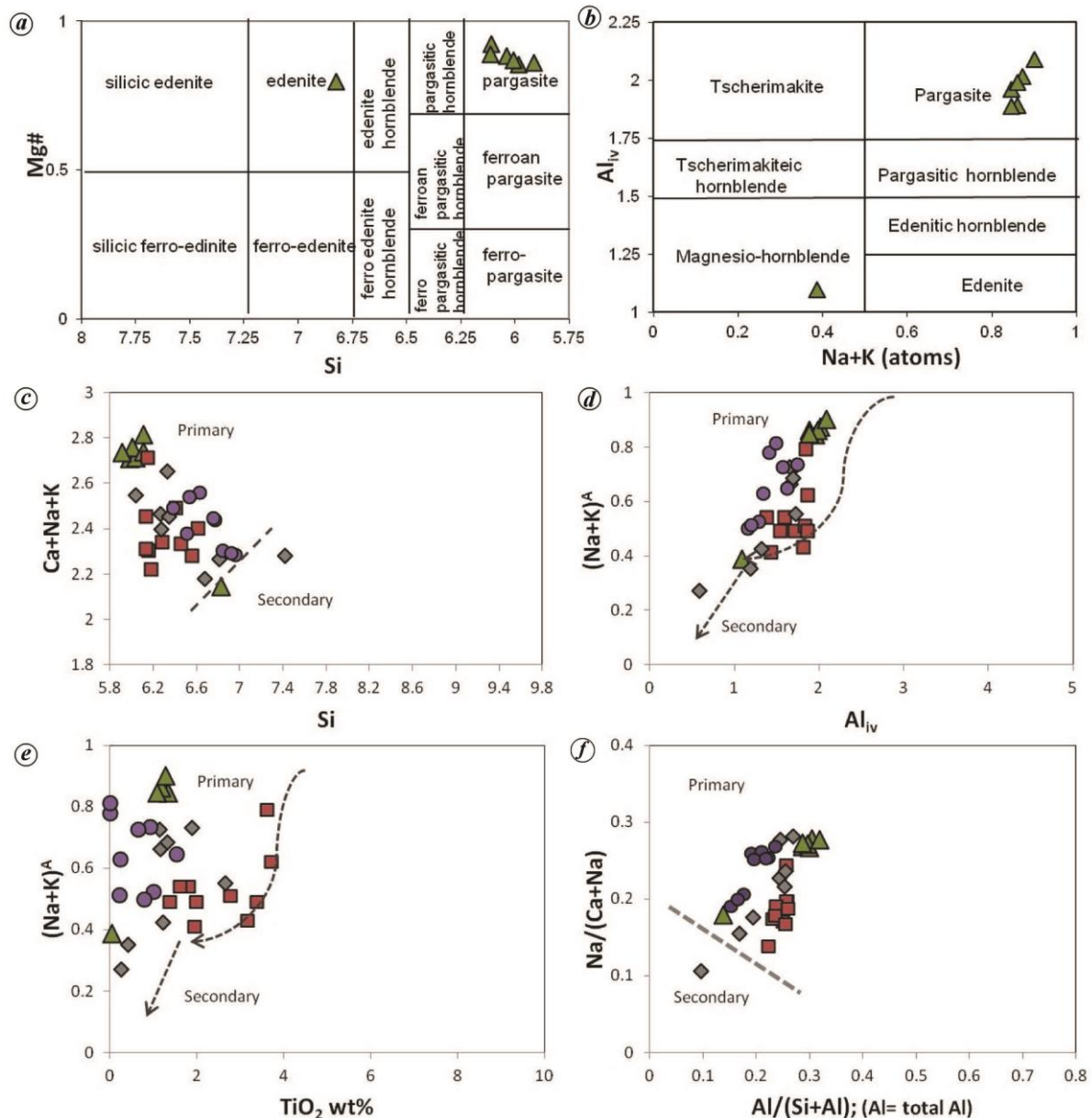


Figure 6. Binary diagrams of amphibole classification in studied pyroxenites. *a*, Mg# versus Si plot⁸². *b*, Al_{iv} versus Na + K plot⁸². *c*, Ca + Na + K (apfu) versus Si (apfu) plot. *d*, Occupancy of Na + K in A-site versus occupancy of Al in the tetrahedral site. *e*, Na + K versus TiO₂ content (wt.%). *f*, (Na/Ca + Na) versus 2Al/(Si + Al) plot; For comparison, various Alaskan-type layered intrusions are shown in the figure; square represents Karayasmak ultramafic–mafic association, Northeast Turkey¹⁰, diamond represents the Gabbro Akarem mafic–ultramafic complex, Eastern desert, Egypt¹³, circle represents the mafic–ultramafic Abu Hamamid intrusion from south eastern desert, Egypt⁷² and triangle represents the amphiboles from the pyroxenites in and around SMUC of the present study.

0.75) for these systems offers better results. For P – T estimation, the homogeneous composition of Opx and Cpx concentration was selected. The moderate re-equilibrium temperatures were obtained from each rock; sample SL-9 showed a temperature range 860–908°C (average 880°C) and pressure of 10.5–11.74 kbar (average 11.17 kbar). Sample SL-4 showed the temperatures range 820–931°C (average 887°C) along with pressure of 10.5–12.23 kbar (average 11.6 kbar). The obtained temperature and pressure were close to the equilibrium temperature of 1022–1088°C

for wehrlite and ~900°C for olivine clinopyroxenite, and pressure of 11 kbar determined by earlier workers from the SMUC⁴⁹.

Discussion

There are several processes described in the literature for the genesis of different types of pyroxenites, which are commonly associated with the ophiolitic complexes Alaskan-type complexes, and layered ultramafic complexes^{7,8,50–54}.

These studies revealed that the pyroxenites commonly intruded the mantle peridotites in the form of thin to thick veins or dykes and layers on various scales and also occurred as cumulates related to crustal magma chambers⁵⁰. Orthopyroxenite, clinopyroxenite and websterites were the important varieties in this category, with a representation of up to 5% in the upper mantle⁵⁵. The subduction of the oceanic lithosphere and recycling of layers within the 'subduction zone through mantle convection', and the interactions of melts or fluids in the upper mantle can also result in the formation of pyroxenites^{12,56–58}. Our field observations suggest that the pyroxenites in and around SMUC represent intrusives in the form of thick veins and dykes within the ultramafic rocks as well as in the basement migmatitic gneiss. Petrography reveals that these are cumulates with the dominance of clinopyroxene and the model composition indicates websterite variety. The clinopyroxene chemistry represents low TiO₂ (<1.0 wt%) and Na₂O (<1.5 wt%) contents, typical of igneous characteristics described from non-alkaline rocks of tholeiitic signature⁵⁹. The presence of low TiO₂ and Na₂O contents also reflects their origin under sub-oceanic source⁶⁰. Various tectonic discrimination diagrams of clinopyroxene chemistry, such as Al_{iv} versus TiO₂ wt%; Ti + Cr versus Ca and Ti versus Al_i plots, reveal their formation under arc environment in subduction zone tectonics (Figure 7 *a*, *c* and *d*)^{61,62}. Similarly, the clinopyroxene composition on a multivariate statistical diagram for discriminating tectonic zones of various groups of mafic–ultramafic rocks represented garnet facies (zones I and II), spinel facies (zones III and IV) and plagioclases facies (zones V, VI and VII), suggesting the island arc origin (VII) for these pyroxenites (Figure 7 *b*)⁶³.

The whole-rock chemistry showed the presence of different Mg# (54–74), coupled with a relatively higher concentration of Cr (1139–2742 ppm) and Ni (139–876 ppm) along with LILE enrichment (Sr, K, Rb, Ba, Th) and HFSE (Ti, Hf, Y, Yb) depletion (Table 1). It also showed negative Nb anomalies (Figure 4 *b* and *c*), with higher ratios of Zr/Nb (7–490) and La/Nb (2–55) and lower ratios of Ce/Pb (0.3–3.4, except for one sample with 14.35) and Th/La (<0.5; Table 1). The characteristic features reported above reflect the arc origin of these pyroxenites derived from subduction zone settings^{64–66}. The geochemical characteristics of pyroxenites are also well correlatable with the geochemistry of mafic magmas of SMUC, which was described earlier as an Alaskan-type complex of Neoproterozoic evolution^{22,67}. It was also reported that ultramafic rocks like dunites from SMUC might have formed through mantle melting, while wehrlites and olivine clinopyroxenites formed through subduction as progressive cumulative products of high magnesium melts⁴⁹. The foregoing strongly indicates that these pyroxenite intrusions might have been closely associated with the arc environment of Alaskan-type. A similar type of arc-related origin of pyroxenites was also described from many Alaskan arc-type environments such as North America-Canada⁶⁸, Tonsina Ultramafic–Mafic

Complex, Alaska¹², ultramafic–mafic complexes of southeastern Alaska⁶, intra-oceanic arc-related cumulates from southern New Zealand and pyroxenite-rich peridotites from Cabo Ortegal-Spain⁶⁹, Galmoenan Pyroxenite–Dunite Plutonic Complex of Koryak Highland, Far East Russia¹⁴, the western part of Cuddapah Basin, Dharwar Craton⁵³, and Alaskan-type complexes of Eastern Desert, Egypt⁷⁰.

The Alaskan-type of intrusions vary in composition and the crystallization history of such magmas remains controversial. One is that they derived from fractionation of alkaline ultramafic parental magmas^{11,71} and the other, through fractional crystallization of H₂O-saturated sub-alkaline island-arc basaltic magmas⁷. Along with other ultramafic rocks from SMUC, these pyroxenites are subjected to metamorphism from low-grade to upper amphibolite facies rather than serpentinization. The higher Mg# content of clinopyroxenes from these pyroxenites indicates that they might have evolved through crystal fractionation–accumulation processes of Mg-rich, hydrous, parental magmas as typical Alaskan-type intrusions (Figure 5 *e*)⁶. Several workers have well documented such Mg-rich mafic and ultramafic intrusions from many Alaskan-type complexes^{6,7,9–11,13}. The Cr–spinel chemistry from dunite as well as peridotites and the Cpx mineral chemistry of gabbro and amphibolites from SMUC point its origin to Alaskan-type^{22,66}. The results of the present study like the plot of Mg# versus Al₂O₃ (Figure 7 *e*) for Cpx from these pyroxenites, substantiate our earlier conclusion of Alaskan-type evolution under relatively high oxygen fugacity (Figure 7 *f*). The occurrence of amphiboles from these intrusions is considered evidence for primary igneous phases. Comparative plots of these amphibole compositions with various Alaskan-type layered ultramafic to mafic intrusions/complexes of magmatic amphiboles indicate close similarities (Figure 6 *c–f*), further strongly supporting the evolution under Alaskan-type^{6,10,13,72}.

The estimated two-pyroxene thermobarometry of these pyroxenites showed re-equilibrium temperatures of 820–932°C with moderate pressure of 10–12 kbar. A similar temperature of 1022–1088°C was also reported from the wehrlite and 900°C from olivine, along with a pressure of 9.8–10.6 kbar for Cpx evolution⁴⁹. It is also suggested that the extracted high magnesian melts were responsible for the generation of wehrlite as well as olivine clinopyroxenite cumulates under the pressure of 11 kbar, which were equilibrated at shallower levels near the base of the crust⁴⁹. The Ti-rich gabbros from SMUC also showed a similar temperature of 893–1014°C and medium pressure of 11–13 kbar respectively⁶⁷. Similar *P–T* conditions of different lithologies obtained for the rocks around SMUC favour a common tectonic history.

It is well explained from many petrogenic models of Alaskan-type of intrusions that a heterogeneous mantle source can be related to variations in subducting slab components of aqueous fluids or melts⁸. These metasomatic agents are the main cause of change in trace elemental concentration and isotopic records of the metasomatized mantle due

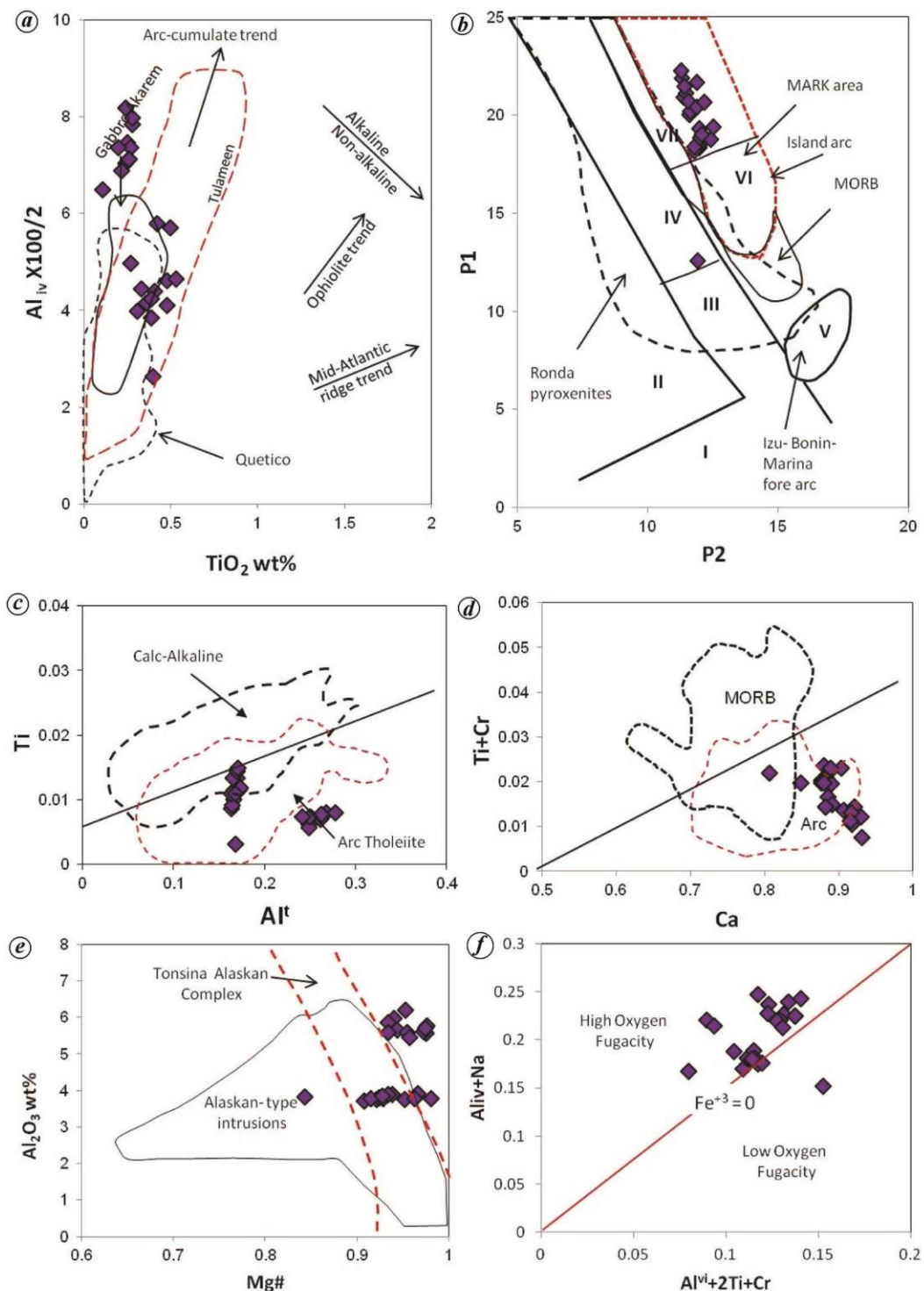


Figure 7. Tectonic classification diagrams of clinopyroxenes of studied pyroxenites. **a.** TiO_2 versus Al_z plot⁶²; the fields of the Alaskan-type complex is after Quetico⁹; Tulameen complex⁸⁴; Gabbr Akarem complex¹³. Non-alkaline and alkaline boundary fields are after⁵⁹ and Al_z refers to the percentage of Al in the tetrahedral sites ($100 \times \text{Al}_{IV}/2$); Arc cumulate, ophiolite and Mid-Atlantic Ridge trends fields from⁸⁵. **b.** P1 versus P2 diagram for pyroxenitic Cpx; fields I–VII and parameters are as defined ref. 63: $\text{P1} = -0.02\text{SiO}_2 + 0.09\text{TiO}_2 + 0.64\text{Al}_2\text{O}_3 + 0.59\text{Cr}_2\text{O}_3 + 1.35\text{FeO} + 9.65\text{MnO} - 0.50\text{MgO} + 0.29\text{CaO} - 2.26\text{Na}_2\text{O} + 8.0$ and $\text{P2} = 0.93\text{TiO}_2 + 0.07\text{Al}_2\text{O}_3 + 1.23\text{Cr}_2\text{O}_3 - 0.46\text{FeO} + 1.74\text{MnO} + 0.36\text{MgO} + 0.10\text{CaO} - 1.66\text{Na}_2\text{O} + 8.0$. Fields: I, Peridotite xenoliths in kimberlites; II, Eclogites and Pyrope-bearing pyroxenites in kimberlites; III, Spinel peridotites; IV, Spinel pyroxenites; V, Island arc peridotites; VI, Island arc pyroxenites and VII, Plagioclase-bearing xenoliths in volcanic rocks from island arcs. Data sources: island arc and mid-ocean ridges⁶³, Izu-Bonin-Mariana forearc⁸⁶, Ronda pyroxenites field after⁸⁷; MARK (Mid-Atlantic Ridge Kane Fracture Zone)⁸⁸. **c.** Ti versus Al_I plot of Cpx⁶¹. **d.** Ca versus Ti + Cr plot⁶¹. **e.** $\text{Mg}\#$ versus Al_2O_3 wt% plot; the field of Alaskan-type intrusions-southeastern Alaska and Tonsina Alaskan ultramafic-mafic rocks after^{6,12} are used for comparison. **f.** $\text{Al}_{IV} + \text{Na}$ versus $\text{Al}_{VI} + 2\text{Ti} + \text{Cr}$ plot for oxygen fugacity determination⁸⁹. Diamond represents Cpx concentration of studied pyroxenites.

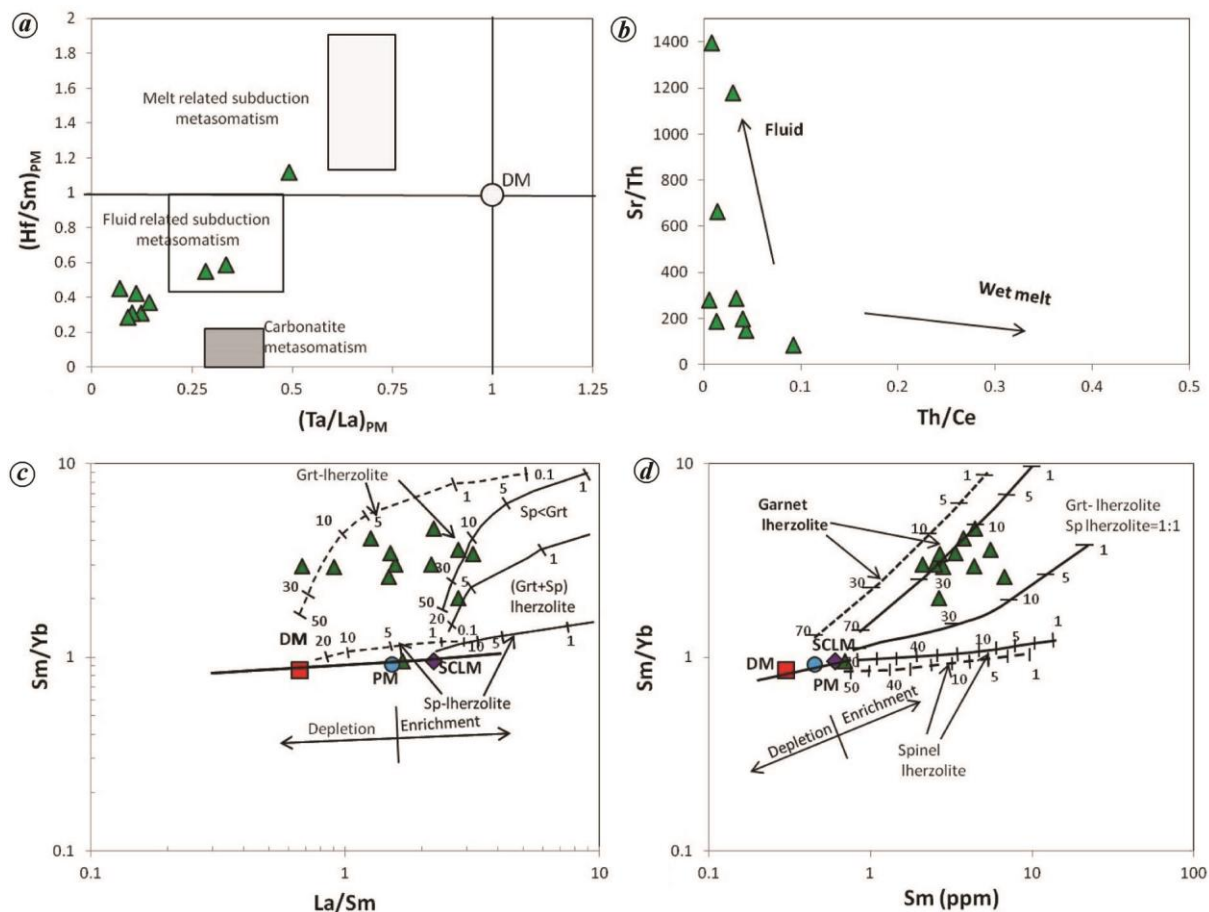


Figure 8. Discrimination plots of whole rock data. *a*, $(\text{Hf}/\text{Sm})_{\text{PM}}$ versus $(\text{Ta}/\text{La})_{\text{PM}}$ after ref. 73. *b*, Sr/Th versus Th/Ce after ref. 73. *c*, Sm/Yb versus Sm . *d*, Sm/Yb versus La/Sm . In (*a*), PM represents the values normalized to the primitive mantle; the subduction and carbonatite-related metasomatism fields after ref. 73. *c* and *d*, The melting curves are after ref. 90, calculated with different starting materials (garnet lherzolite, garnet-spinel lherzolite and spinel lherzolite) using the non-modal batch melting equations. The dashed and solid lines represent the melting trends for depleted mantle (DM, $\text{Sm} = 0.3$ ppm and $\text{Sm}/\text{Yb} = 0.86$, after ref. 91) and enriched sub-continental lithospheric mantle (SCLM, $\text{Sm} = 0.6$ ppm and $\text{Sm}/\text{Yb} = 0.96$, after ref. 75) respectively. Partition coefficients are from the compilation of earlier workers⁹¹. Degrees of partial melting are based on the given sources which are marked beside the curves. Square symbol represents Depleted Mantle concentration, Circle represents PM concentration, Diamond represents SCLM concentration, and triangles represents the concentrations of studied pyroxenites.

to the preference of LILE over HFSE to enter aqueous fluids⁸. This results in recognition of a host of well-recorded elemental ratios capable of monitoring potential fluid contributions to the magma sources. The (Ta/La) and (Hf/Sm) primitive normalized ratios of these pyroxenite intrusions were 0.1–0.5 (except for one sample of 2.1) and 0.31–1.3 respectively, on plotting with $\text{Hf}/\text{Sm}_{\text{PM}}$ versus $\text{Ta}/\text{La}_{\text{PM}}$ (Figure 8*a*)⁷³, they reflect the dominance of metasomatized fluid addition from the mantle source. The Sr/Th ratios were highly elevated and Sr/Th versus Th/Ce plot (Figure 8*b*)⁷⁴ also reveals a major contribution from an aqueous fluid component for pyroxenite magmas. Distinctive elemental abundances and their ratios in the basaltic magmas are helpful for the characterization of the source mineralogy of the mantle. In this aspect, such elemental abundances like REE concentrations and their ratios are useful proxies because of their progressive increase incompatibility from LREE to HREE for characterization of source mineralogy⁷⁵.

The La/Sm and Sm/Yb ratios of these pyroxenites varied from 0.67 to 3.16 and 0.95 to 3.6 respectively. On La/Sm versus Sm/Yb and Sm/Yb versus Sm plots (Figure 8*c* and *d*) respectively, these intrusions fall between the garnet and spinel lherzolite melting trajectories, suggesting the presence of garnet-dominated mineral assemblages in their source region with varying degrees of partial melting of a fertile subcontinental lithospheric mantle source.

CSZ has been described as a Neoproterozoic Gondwana suture and its further westward continuation has been observed in Madagascar (Betsimisaraka suture) as well as in the African continent²⁷. Neoproterozoic, subduction-related magmatism associated with high-grade assemblages, including two-pyroxene granulites, charnockites, ophiolites and granitoids of arc environment of equivalent age groups, has been described by several workers within the CSZ^{17,18,22,25–28}. The ultrapotassic rocks like shonkinites with ages of 808 ± 18 Ma were also described from SMUC⁴⁰. The U–Pb zircon

ages from quartz monzonite intruding hornblendites from SMUC also yielded similar ages of 819 ± 2.4 Ma (ref. 22), and the evolution of the Complex has been described as Neoproterozoic Alaskan-type. Further, Neoproterozoic (~800 Ma) ages of dismembered ophiolites and arc magmatism have been reported from many parts of the CSZ^{18,30,76}. Cryogenian alkaline magmatism of similar age (~800 Ma) equivalents was also reported from the western parts of CSZ⁷⁷. All these evidences strongly reveal a major Neoproterozoic event of subduction-related arc volcanism at the interface of the SGT and the southern margin of the Dharwar Craton, resulting in the development of pyroxenites in and around SMUC, genetically related to the evolution of CSZ.

Conclusion

The variety pyroxenite dykes in and around SMUC are of websterite and consist primarily of Cpx, along with Opx, primary amphiboles, magnetites, ilmenite and spinels. The geochemical characteristics of these pyroxenites indicate an enrichment of LILE and depletion of HFSE with negative Nb anomalies similar to the arc-related origin of magmas. The Cpx mineral chemistry reveals the tholeiitic signature of the magmas that are derived under the arc environment of Alaskan-type evolution in association with the interactions of subduction-related fluids. The two-pyroxene thermobarometry shows relatively lower re-equilibrium temperatures of 820–932°C, and moderate to slightly higher pressures of 10.5–12 kbar for their evolution. The geochemical results of pyroxenites from the present study in and around SMUC are similar to those of amphibolites and gabbros of the SMUC. The above results together with the available ages from the complex suggest that there might be a possible syn-tectonic evolution of these pyroxenite intrusions along with the host rocks in and around the complex during the Neoproterozoic.

- Dick, H. J. B. and Sinton, J. M., Compositional layering in Alpine peridotites: evidence for pressure solution creep in the mantle. *J. Geol.*, 1979, **87**, 403–416.
- Allegre, C. J. and Turcotte, D. L., Implications of a two-component marble cake mantle. *Nature*, 1986, **23**, 123–127.
- Garrido, C. J. and Bodinier J. L., Diversity of mafic rocks in the Ronda peridotite: evidence for pervasive melt-rock reaction during heating of subcontinental lithosphere by upwelling asthenosphere. *J. Petrol.*, 1999, **40**(5), 729–754.
- Medaris Jr, L. G., Beard, B. L., Johnson, C. M., Valley, J. W., Spicuzza, M. J., Jelínek, E. and Mísar, Z., Garnet pyroxenite and eclogite in the Bohemian Massif: geochemical evidence for Variscan recycling of subducted lithosphere. *Geol. Rundsch.*, 1995, **84**, 489–505.
- Dowens, H., Origin and significance of spinel and garnet pyroxenites in the shallow lithospheric mantle in Western Europe and NW Africa. *Ophioliti*, 2005, **30**, 165–166.
- Himmelberg, G. R. and Loney, R. A., Characteristics and petrogenesis of Alaskan-type ultramafic–mafic intrusions, southeastern Alaska. *US Geol. Surv. Prof. Pap.*, 1995, 1564.
- Helmy, H. M. *et al.*, Petrology and Sm–Nd dating of the Genina Gharbia Alaskan-type complex (Egypt): insights into deep levels of Neoproterozoic island arcs. *Lithos*, 2014, **198–199**, 263–280.
- Yuan, L., Zhang, X., Yang, Z., Lu, Y. and Chen, H., Paleoproterozoic Alaskan-type ultramafic–mafic intrusions in the Zhongtiao mountain region, North China Craton: petrogenesis and tectonic implication. *Precambrian Res.*, 2017, **296**, 39–61.
- Pettigrew, N. T. and Hattori, K. H., The Quetico intrusions of Western Superior Province: Neo-Archean examples of Alaskan/Ural-type mafic–ultramafic intrusions. *Precambrian Res.*, 2006, **149**, 21–42.
- Eyuboglu, Y., Dilek, Y., Bozkurt, E., Bektas, O., Rojay, B. and Sen, C., Structure and geochemistry of the Alaskan-type ultramafic–mafic complex in the Eastern Pontides, NE Turkey. *Gondwana Res.*, 2010, **18**, 230–252.
- Irvine, T. N., Petrology of the Duke Island ultramafic complex, Southeastern Alaska. *Geol. Soc. Am. Mem.*, 1974, **138**, 240.
- De Bari, S. M. and Coleman, R. G., Examination of the deep levels of an island arc: evidence from the Tonsina ultramafic–mafic assemblage, Tonsina, Alaska. *J. Geophys. Res.*, 1989, **94**, 4373–4391.
- Helmy, H. M. and El Mahallawi, M. M., Gabbro Akarem mafic–ultramafic complex, Eastern Desert, Egypt: a late Precambrian analogue for Alaskan-type complexes. *J. Mineral. Petrol.*, 2003, **7**, 85–108.
- Batanova, V. G., Pertsev, A. N., Kamenetsky, V. S., Ariskin, A. A., Mochalov, A. G. and Sobolev, A. V., Crustal evolution of island-arc ultramafic magma: Galmoenan Pyroxenite–Dunite Plutonic Complex, Koryak Highland (Far East Russia). *J. Petrol.*, 2005, **46**(7), 1345–1366.
- Murthy, S. R. N., Petrology of ultramafic rocks of the Chalk Hills, Salem, Tamil Nadu. *Rec. Geol. Surv. India*, 1979, **112**, 15–35.
- Gopalakrishnan, K., An overview of Southern Granulites Terrain of Tamil Nadu: constraints in reconstruction of Precambrian assembly of Gondwanaland. In Proceedings of *Gondwana 9th International Symposium*, Oxford and IBH Publications Co Ltd, New Delhi, 1994, vol. 2, pp. 1003–1026.
- GSI, *Geology and Mineral Resources of Tamil Nadu and Pondicherry, Part-VI*, Geological Survey of India, Kolkata, Miscell. Pub., 2006 No. 30, 2006.
- Yellappa, T., Chetty, T. R. K., Tsunogae, T. and Santosh, M. Manamedu complex: geochemical constraints on Neoproterozoic suprasubduction zone ophiolite formation within Gondwana suture in southern India. *J. Geodyn.*, 2010, **50**, 268–285.
- Yellappa, T. *et al.*, A Neoproterozoic dismembered ophiolite complex from southern India: geochemical and geochronological constraints on its suprasubduction origin. *Gondwana Res.*, 2012, **21**, 245–265.
- Yellappa, T., Venkatasivappa, V., Koizumi, T., Chetty, T. R. K., Santosh, M. and Tsunogae, T., The mafic–ultramafic complex of Aniyapuram, Cauvery Suture Zone, southern India: petrological and geochemical constraints for Neoproterozoic suprasubduction zone tectonics. *J. Asian Earth Sci.*, 2014, **95**, 81–98.
- Santosh, M., Shaji, E., Tsunogae T., Rammohan M., Satyanarayanan, M. and Horie K., Neoproterozoic suprasubduction zone ophiolite from Agali hill, southern India: petrology, zircon SHRIMP U–Pb geochronology, geochemistry and tectonic implications. *Precambrian Res.*, 2013, **231**, 301–324.
- Yellappa, T., Santosh, M. and Manju, S., The mafic–ultramafic complex of Salem, southern India: an analogue for Neoproterozoic Alaskan-type complex. *Geol. J.*, 2019, **54**, 3017–3040.
- Ramakrishnan, M. and Vaidyanathan, R., *Geology of India*, 2008, Geological Society of India, Bangalore, 2008, vol. 1, p. 426.
- Chetty, T. R. K., *Proterozoic Orogens of India: A Critical Window to Gondwana*, Elsevier Publication, Amsterdam, The Netherlands, 2017, p. 426.
- Ghosh, J. G., Maarten, De Wit, R. E. and Zartman, R. E., Age and tectonic evolution of Neoproterozoic ductile shear zones in the Southern Granulite Terrane of India, with implications for Gondwana studies. *Tectonics*, 2004, **23**, TC3006.

26. Santosh, M., Maruyama, S. and Sato, K., Anatomy of a Cambrian suture in Gondwana: Pacific-type orogeny in southern India. *Gondwana Res.*, 2009, **16**, 321–341.
27. Collins, A. S., Clark, C. and Plavsa, D., Peninsular India in Gondwana: the tectonothermal evolution of the Southern Granulite Terrane and its Gondwana counterparts. *Gondwana Res.*, 2014, **25**, 190–203.
28. Plavsa, D., Collins, A. S., Payne, J. L., Foden, J. D., Clark, C. and Santosh, M., Detrital zircons in basement metasedimentary protoliths unveil the origins of southern India. *Geol. Soc. Am. Bull.*, 2014, **126**, 791–812.
29. Drury, S. A. and Holt, R. W., The tectonic framework of the South Indian Craton: a reconnaissance involving LANDSAT imagery. *Tectonophysics*, 1980, **65**, T1–T5.
30. Santosh, M., Xiao, W. J., Tsunogae T., Chetty, T. R. K. and Yellappa, T., The Neoproterozoic subduction complex in southern India: SIMS zircon U–Pb ages and implications for Gondwana assembly. *Precambrian Res.*, 2012, **192–195**, 190–208.
31. Raith, M., Srikantappa, C., Buhl, D. and Kuhler, H., The Nilgiri enderbites, South India: nature and age constraints on protolith formation, high-grade metamorphism and cooling history. *Precambrian Res.*, 1999, **98**, 129–150.
32. Tsunogae, T., Santosh, M. and Dubessy, J., Fluid characteristics of high-to ultrahigh-temperature metamorphism in southern India: a quantitative Raman spectroscopic study. *Precambrian Res.*, 2008, **162**, 198–211.
33. Koizumi, T., Tsunogae, T., Santosh, M. and Chetty, T. R. K., Petrology and zircon U–Pb geochronology of metagabbros from a mafic-ultramafic suite at Aniyapuram: Neoproterozoic to Early-Paleoproterozoic convergent margin magmatism and Middle-Neoproterozoic high-grade metamorphism in southern India. *J. Asian Earth Sci.*, 2014, **95**, 51–64.
34. Chetty, T. R. K. and Bhaskar Rao, Y. J., Behavior of stretching lineations in the Salem–Attur shear belt, Southern Granulite Terrane, South India. *J. Geol. Soc. India*, 1998, **52**, 443–448.
35. Bhadra, B. K., Ductile shearing in Attur shear zone and its relation with Moyar shear zone, South India. *Gondwana Res.*, 2000, **3**, 361–369.
36. Jain, A. K., Singh, S. and Manickavasagam, Intra-continental shear zones in the Southern Granulite Terrane: their kinematics and evolution. *Geol. Soc. India Mem.*, 2003, **50**, 225–253.
37. Biswal, T. K., Thirukumaran, V., Kamleshwar, R., Bandyapadhya, K., Sundaralingam, K. and Mandal, A. K., A study of mylonites from parts of the Salem–Attur Shear Zone (Tamil Nadu) and its tectonic implications. *J. Geol. Soc. India*, 2010, **75**, 128–136.
38. Naha, K. and Srinivasan, R., Nature of the Moyar and Bhavani shear zones, with a note on their implication on the tectonics of the southern Indian Precambrian shield. *Proc. Indian Acad. Sci., Earth Planet. Sci.*, 1996, **105**, 173.
39. Basu, A. K., An interim report on the investigation for magnesite in Chalk Hills area, Salem district, Tamil Nadu. Report of Geological Survey of India, Kolkotta, FS, 1978–79, 1982, pp. 1–28.
40. He, X. F., Santosh, M., Zhang, Z. M., Tsunogae, T., Chetty, T. R. K., Ramhohan, M. and Anbazhagan, S., Shonkinites from Salem, southern India: implications for Cryogenian alkaline magmatism in rift-related setting. *J. Asian Earth Sci.*, 2015, **113**, 812–825.
41. Balaram, V. and Rao, T. G., Rapid determination of REEs and other trace elements in geological samples by microwave acid digestion and ICP-MS. *At. Spectrosc.*, 2003, **24**, 206–212.
42. Whattam, S. A., Cho, M. and Smith, I. E. M., Magmatic peridotites and pyroxenites, Andong Ultramafic Complex, Korea: geochemical evidence for supra-subduction zone formation and extensive melt-rock interaction. *Lithos*, 2011, **127**, 599–618.
43. Green, D. H. and Ringwood, A. E., The stability fields of aluminous pyroxene peridotite and garnet peridotite composite and their relevance in upper mantle structure. *Earth Planet. Sci. Lett.*, 1967, **3**, 151–160.
44. Giret, A., Bonin, B. and Léger, J. M., Amphibole compositional trends in oversaturated and under saturated alkaline plutonic ring complexes. *Can. Mineral.*, 1980, **18**, 481–495.
45. Rosalind, T. H., Experimental studies of amphibole stability; phase relations and compositions of amphiboles produced in studies of the melting behavior of rocks. *Rev. Mineral. Geochem.*, 1982, **9B**(1), 279–353.
46. Brey, G. and Köhler, T., Geothermobarometry in four-phase lherzolites II. New thermobarometers and practical assessment of existing thermobarometers. *J. Petrol.*, 1990, **31**, 1353–1378.
47. Putirka, K., Thermometers and barometers for volcanic systems. *Rev. Mineral. Geochem.*, 2008, **69**, 61–120.
48. Nimis, P. and Ulmer, P., Clinopyroxene geobarometry of magmatic rocks, Part 1: an expanded structural geobarometer for anhydrous and hydrous, basic and ultrabasic systems. *Contrib. Mineral. Petrol.*, 1998, **133**, 122–135.
49. Maitra, M., Bose, M. K. and Ray, J., Interpretative mineral chemistry of ultramafic rocks of Chalk Hills, Tamil Nadu. *J. Geol. Soc. India*, 2006, **68**, 831–840.
50. Berly, T. J., Hermann, J., Arculus, R. J. and Lapierre, H., Suprasubduction zone pyroxenites from San Jorge and Santa Isabel (Solomon Islands). *J. Petrol.*, 2006, **7**, 1531–1555.
51. Bodinier, J. L., Garrido, M. C., Chanefo, I., Bruguier, O. and Ger-villa, F., Origin of pyroxenite–peridotite veined mantle by refertilization reactions: evidence from the Ronda peridotite (southern Spain). *J. Petrol.*, 2008, **49**(5), 999–1025.
52. Rogkala, A., Petrounias, P., Tsikouras, B. and Hatzipanagiotou, K., New occurrence of pyroxenites in the Veria-Naousa ophiolite (North Greece): implications on their origin and petrogenetic evolution. *Geosciences*, 2017, **7**(92), 1–23.
53. Sharma, A., Rohit Kumar, G., Chalpathi Rao, N. V., Rahaman, W., Pandit, D. and Sahoo, S., Arc-related pyroxenites derived from a long-lived Neoproterozoic subduction system at the southwestern margin of the Cuddapah basin: geodynamic implications for the evolution of eastern Dharwar Craton, Southern India. *J. Geol.*, 2019, **127**, 567–591.
54. Yellappa, T., Koizumi, T. and Tsunogae, T., Geochemical constraints on pyroxenites from Aniyapuram complex, Cauvery Suture Zone, Southern India: suprasubduction zone origin. *J. Earth Syst. Sci.*, 2021, **130**(11), 1–24.
55. Hirschmann, M. and Stolper, E. M., A possible role for garnet pyroxenite in the origin of the garnet signature in MORB. *Contrib. Mineral. Petrol.*, 1996, **124**, 185–208.
56. Kornprobst, J., Piboule, M., Roden, M. and Tabit, A., Corundum-bearing garnet clinopyroxenites at Beni-Bousera (Morocco) ϕ -original plagioclase-rich gabbros recrystallized at depth within the mantle. *J. Petrol.*, 1990, **31**, 717–745.
57. Pearson, D. G., Davies, G. R. and Nixon, P. H., Geochemical constraints on the petrogenesis of diamond facies pyroxenites from the Beni Bousera peridotite massif, North Morocco. *J. Petrol.*, 1993, **34**, 125–172.
58. Wang, Z., Wilde, S. A. and Wan, J., Tectonic setting and significance of 2.3–2.1 Ga magmatic events in the Trans-North China Orogen: new constraints from the Yanmenguan mafic–ultramafic intrusion in the Hengshan–Wutai–Fuping area. *Precambrian Res.*, 2010, **178**, 27–42.
59. Le Bas, M. J., The role of aluminium in igneous clinopyroxenes with relation to their parentage. *Am. J. Sci.*, 1962, **260**, 267–288.
60. Delavari, M., Amini, S., Saccani, E. and Beccaluva, L., Geochemistry and petrogenesis of mantle peridotites from the Nehabandan ophiolitic complex, eastern Iran. *J. Appl. Sci.*, 2009, **9**, 2671–2687.
61. Leterrier, J., Maury, R. C., Thonon, P., Girard, D. and Marechal, M., Clinopyroxene composition as a method of identification of the magmatic affinities of paleovolcanic series. *Earth Planet. Sci. Lett.*, 1982, **59**, 139–154.
62. Beccaluva, L., Macciotta, G., Piccardo, G. B. and Zeda, O., Clinopyroxene composition of ophiolitic basalts as petrogenetic indicators. *Chem. Geol.*, 1989, **77**, 165–182.

63. Koloskov, A. V. and Zharinov, S. E., Multivariate statistical analysis of clinopyroxene compositions from mafic and ultramafic xenoliths in volcanic rocks. *J. Petrol.*, 1993, **34**, 173–185.
64. Pearce, J. A., Lippard, L. S. and Roberts, S., Characteristics and tectonic significance of suprasubduction zone ophiolites. *Geol. Soc. London Spec. Publ.*, 1984, **16**, 77–94.
65. Tatsumi, Y., Hamilton, D. L. and Nesbitt, R. W., Chemical characteristics of fluid phase released from a subducted lithosphere and origin of arc magmas: evidence from high pressure experiments and natural rock. *J. Volcanol. Geotherm. Res.*, 1986, **29**, 293–309.
66. Polat, A., Appel, P. W. U. and Fryer, B. J., An overview of the geochemistry of Eoarchean to Mesoarchean ultramafic to mafic volcanic rocks, SW Greenland: implications for mantle depletion and petrogenetic processes at subduction zones in the early Earth. *Gondwana Res.*, 2011, **20**, 255–283.
67. Yellappa, T., High Ti-bearing gabbros from Chalk hills of Salem, Southern Granulite Terrane, India. *J. Geol. Soc. India*, 2021, **97**, 21–34.
68. Snoko, A. W., Quick, J. E. and Bowman, H. R., Bear Mountain igneous complex, Klamath Mountains, California: an ultrabasic to silicic calcalkaline suite. *J. Petrol.*, 1981, **22**, 501–552.
69. Spandler, C. J., Arculus, R. J., Eggins, S. M., Mavrogenes, J. A., Price, R. C. and Reay, A. J., Petrogenesis of the Green Hills Complex, Southland, New Zealand: magmatic differentiation and cumulate formation at the roots of a Permian island-arc volcano. *Contrib. Mineral. Petrol.*, 2003, **144**, 703–721.
70. Abdallah, S. E., Ali, S. and Obeid, M. A., Geochemistry of an Alaskan-type mafic-ultramafic complex in Eastern Desert, Egypt: new insights and constraints on the Neoproterozoic island arc magmatism. *Geosci. Front.*, 2019, **10**(3), 941–955.
71. Irvine, T. N., *Bridget Cove Volcanics, Juneau Area, Alaska: Possible Parental Magma of Alaskan-Type Ultramafic Complexes*, Yearbook 72, Carnegie Institution of Washington, USA, 1973, pp. 478–491.
72. Farahat, E. S. and Helmy, H. M., Abu Hamamid Neoproterozoic Alaskan-type complex, southeastern Desert, Egypt. *J. Afr. Earth Sci.*, 2006, **45**, 187–197.
73. La Flèche, M. R., Camiré, E. G. and Jenner, G. A., Geochemistry of post-Acadian, carboniferous continental intraplate basalts from the Maritimes Basin, Magdalen Islands, Québec, Canada. *Chem. Geol.*, 1998, **148**, 115–136.
74. Turner, S., Caulfield, J., Turner, M., Keken P., Maury, R., Sandiford, M. and Prouteau, G., Recent contribution of sediments and fluids to the mantle's volatile budget. *Nature Geosci.*, 2012, **5**, 50–54.
75. Aldanmaz, E., Pearce, J. A., Thirlwall, M. F. and Mitchell, J. G., Petrogenetic evolution of late Cenozoic, post-collision volcanism in western Anatolia, Turkey. *J. Volcanol. Geotherm. Res.*, 2000, **102**, 67–95.
76. Teale, W., Collins, A., Foden, J., Payne, J., Plavsa, D., Chetty, T. R. K., Santosh, M. and Fanning, M., Cryogenian (~830 Ma) mafic magmatism and metamorphism in the northern Madurai Block, southern India: a magmatic link between Sri Lanka and Madagascar. *J. Asian Earth Sci.*, 2011, **42**, 223–233.
77. Santosh, M., Yang, Q. Y., Rammohan, M., Tsunogae, T., Shaji, E. and Satyanarayanan, M., Cryogenian alkaline magmatism in the Southern Granulite Terrane, India: petrology, geochemistry, zircon U–Pb ages and Lu–Hf isotopes. *Lithos*, 2014, **208–209**, 430–445.
78. GSI, *Geological Map of Kerala, Tamil Nadu and Pondicherry (1 : 500,000)*, Geological Survey of India, Calcutta, 1995.
79. Xiong, Q., Zheng, J. P., Griffin, W. L., O'Reilly, S. Y. and Pearson, N. J., Pyroxenite dykes in orogenic peridotite from North Qaidam (NE Tibet, China) track metasomatism and segregation in the mantle wedge. *J. Petrol.*, 2014, **55**, 2347–2376.
80. Sun, S. S. and McDonough, W. F., Chemical and isotope systematics of oceanic basalts: implications for mantle composition and processes. *Geol. Soc. London, Spec. Publ.*, 1989, **42**, 313–345.
81. Morimoto, N. *et al.*, Nomenclature of pyroxenes. *Am. Mineral.*, 1988, **73**, 1123–1133.
82. Leake, B. E., Nomenclature of amphiboles. *Mineral. Mag.*, 1978, **42**, 533–563.
83. Aoki, K. I. and Kushiro, I., Some clinopyroxenes from ultramafic inclusions in Dreiser Weiher, Eifel. *Contrib. Mineral. Petrol.*, 1968, **18**, 326–337.
84. Rublee, V. J., Chemical petrology, mineralogy and structure of the Tulameen Complex, Princeton Area, British Columbia. MSc thesis, University of Ottawa, Ontario, Canada, 1994, p. 183.
85. Loucks, R. R., Discrimination of ophiolitic from non-ophiolitic ultramafic-mafic allochthons in orogenic belts by the Al/Ti ratios in clinopyroxene. *Geology*, 1990, **18**, 346–349.
86. Parkinson, I. J. and Pearce, J. A., Peridotites from the Izu–Bonin–Mariana fore arc (ODP Leg 125): evidence for mantle melting and melt–mantle interaction in a suprasubduction zone setting. *J. Petrol.*, 1998, **39**(1), 577–1618.
87. Obata, M., Petrology and petrogenesis of the Ronda High-Temperature peridotite Intrusion, southern Spain. Ph D thesis, Massachusetts Institute of Technology, Cambridge, MA, USA, 1977, p. 247.
88. Gaggero, L. and Cortesogno, L., Metamorphic evolution of oceanic gabbros: recrystallization from solidus to hydrothermal conditions in the MARK area (ODP Leg 153). *Lithos*, 1997, **40**, 105–131.
89. Schweitzer, E. L., Papike, J. J. and Bence, A. E., Statistical analysis of clinopyroxenes from deep-sea basalts. *Am. Mineral.*, 1979, **64**, 501–513.
90. Shaw, D. M., Trace element fractionation during anatexis. *Geochim. Cosmochim. Acta*, 1970, **34**, 237–243.
91. Mckenzie, D. P. and Onions, R. K., Partial melt distribution from inversion of rare earth element concentrations. *J. Petrol.*, 1991, **32**, 1021–1091.

ACKNOWLEDGEMENTS. I thank the Director, CSIR-National Geophysical Research Institute, Hyderabad, for providing the necessary facilities, encouragement and permission to publish this paper. I also thank my colleagues Dr Khesava Krishna, Dr S. Savanth, Dr M. Satyanarayanan, Dr E. V. S. S. K. Babu, Ms S. Manju and Mr B. Naveen Kumar for their help during XRF, ICPMS and EPMA analysis; thanks to Dr T. R. K. Chetty, anonymous reviewers and Prof. Somnath Das Gupta, handling editor for their useful suggestions in the improvement of the manuscript. This work is a part of the sponsored project (ref: EEQ/2018/001004) under the Department of Science and Technology, Government of India.

Received 3 July 2021; re-revised accepted 11 June 2022

doi: 10.18520/cs/v123/i8/1005-1019